



1 Spatiotemporal Variability and Environmental Controls on Aquatic Methane Emissions in an Arctic  
 2 Permafrost Catchment

3 Michael W. Thayne<sup>1</sup>, Karl Kemper<sup>1,2</sup>, Christian Wille<sup>1</sup>, Aram Kalhori<sup>1</sup>, & Torsten Sachs<sup>1,3</sup>

4 <sup>1</sup> GFZ Helmholtz Centre for Geosciences, Potsdam, Germany

5 <sup>2</sup> Department of Geosciences, University of Cologne, Cologne, Germany

6 <sup>3</sup> Institute of Geoecology, Technical University of Braunschweig, Braunschweig, Germany

7 Correspondence email: Michael W. Thayne (m\_thayne@me.com)

## 8 Abstract

9 Understanding spatiotemporal dynamics and drivers of methane (CH<sub>4</sub>) fluxes from rapidly changing  
 10 permafrost regions is critical for improving our understanding of such changes. Between May and  
 11 August 2023 and 2024, we measured CH<sub>4</sub> using floating chambers in a small Arctic permafrost  
 12 catchment on Disko Island, Greenland. Diffusive and ebullitive fluxes were derived from 707  
 13 measurements using a semi-automated algorithm incorporating boosted regression trees and  
 14 generalized additive models. Highest fluxes occurred in streams and along lakeshores associated  
 15 with inlets. Diffusion processes dominated (98%), while 2% were split between ebullition and  
 16 uptake. Median diffusive fluxes were 5.0 nmol m<sup>-2</sup>s<sup>-1</sup>, (-0.1 to 271.8), peaking at ice-break. Ebullition  
 17 had a median of 939 nmol m<sup>-2</sup>s<sup>-1</sup> (5.2 - 14,893), but did not impact overall fluxes. Model results  
 18 suggest thaw-season fluxes reflected meteorology and soil wetness effects, later shifting to  
 19 biogeochemical controls: dissolved organic matter, oxygen saturation, and pH. Spatial variability  
 20 arose from patchy conditions shaped by substrate, primary producers and microbial assemblages.

## 21 1 Introduction

22 Permafrost regions across the Arctic store substantial amounts of carbon. Climate warming  
 23 is rapidly changing permafrost regions and consequently their carbon storage dynamics, creating a  
 24 critical climate feedback mechanism (Schuur et al., 2015; Miner et al., 2022). At current warming  
 25 rates, models project approximately 77% of shallow permafrost will be lost by 2100 (Fox-Kemper et  
 26 al. 2021, suggesting large implications for the global carbon budget and how carbon emissions are  
 27 distributed across permafrost landscapes. The underlying issue is that thawing permafrost can  
 28 release previously frozen organic matter, delivering labile nutrients to soil microbes which produce  
 29 carbon as a result of their metabolic processes (Schuur et al., 2015; Keskitalo et al., 2021; Olefeldt et  
 30 al., 2021). Subtle changes in microbial processes in soils can enhance positive feedback mechanisms  
 31 which compounds atmospheric warming. Lateral movement of water through active layer soils is a  
 32 critical pathway for CH<sub>4</sub> emissions from surface waters (Street et al., 2016; Olid et al., 2021, 2022;  
 33 Fazi et al., 2021). Hydrological and catchment system dynamics in particular play a critical role in  
 34 distributing dissolved carbon throughout permafrost environments. Catchment systems, such as  
 35 thermokarst lakes and wetlands, have been shown to be “hotspots” for CH<sub>4</sub> release, where daily  
 36 emission rates between 10 and 200 mg m<sup>-2</sup>d<sup>-1</sup> have been reported (Walter Anthony et al., 2018;  
 37 Elder et al., 2020). However, while localized high emissions have been reported, the overall  
 38 contribution of Arctic and permafrost freshwater bodies to global methane budgets is fairly low at 2-  
 39 6% when compared to other ecoregions such as the tropics at 64% (Bastviken et al., 2004; Saunois et  
 40 al., 2016; Virkkala et al., 2024). Nonetheless, with such drastic change expected, well designed field  
 41 studies exploring which processes are the most important for governing CH<sub>4</sub> emissions from



42 permafrost regions, are critical data sources for validating climate models and simulations (Bartsch  
43 et al. 2025).

44 Carbon dynamics in permafrost regions have been shown to be governed by interactions  
45 between soil, vegetation, hydrology, and atmospheric processes (Walter Anthony et al., 2012;  
46 Virkkala et al., 2024; Yuan et al., 2024; Kleber et al. 2025). Located on the central-west coast of  
47 Greenland, Qeqertarsuaq, also known as Disko Island, has become an important data point for  
48 understanding environmental interactions which govern Arctic tundra carbon dynamics. The island  
49 provides a natural laboratory for observing interactions between permafrost, vegetation, microbial  
50 activity and aquatic ecosystems (Humlum, 1998; Humlum et al., 1999; Callaghan et al., 2011;  
51 Christiansen et al., 2015; D'Imperio et al., 2017). Previous work from the study area has suggested  
52 shifting hydrology, historic permafrost thaw, nutrient cycling, and microbial activity in the active and  
53 permafrost layers as possible drivers of CH<sub>4</sub> fluxes from surface water bodies (Zastruzny et al., 2017;  
54 Kluge et al., 2021; Stevenson et al., 2021; Juncher Jørgensen et al., 2024). These studies highlight the  
55 interconnectedness of terrestrial and aquatic ecosystems, and the effect they may have on CH<sub>4</sub>  
56 fluxes from lakes and streams on Disko Island. There is yet to be an extensive study on CH<sub>4</sub> fluxes  
57 from the island's lakes and streams. However, it has been suggested that permafrost thaw and  
58 warming air temperatures may have an effect on greenhouse gas fluxes (Kluge et al., 2021; Juncher  
59 Jørgensen et al., 2024). Soil warming experiments and studies of increased snow cover in winter  
60 were shown to regulate carbon fluxes through accelerated carbon turnover (Ravn et al., 2020; Xu et  
61 al., 2021). Carbon fluxes are further controlled by plant uptake and through microbial activity  
62 regulating the availability of nutrients and subsequent CH<sub>4</sub> production (Laanbroek, 2010; Liebner et  
63 al., 2011; D'Imperio et al., 2017). Sedimentary processes in lakes were shown to store carbon, while  
64 methanotroph and methanogen microbial assemblages along an upland-wetland environmental  
65 gradient were shown to be important for consuming and emitting CH<sub>4</sub>, respectively. Therefore,  
66 freshwater ecosystems systems play a critical role storing, producing, and emitting CH<sub>4</sub> (Christiansen  
67 et al., 2015; Žárský et al., 2018; Stevenson et al., 2021).

68 The hydrology of Disko Island is strongly influenced by past volcanic activity during the  
69 Paleocene epoch. With extensive basaltic lava flows characterizing the landscape, the islands terrain  
70 is formed by the Maligât and Vaigat Formations, which are comprised of highly permeable layers of  
71 basalt interbedded with fluvial and lacustrine sediments (Westergaard-Nielsen et al., 2020; Larsen &  
72 Larsen, 2022). The high permeability of these geologic formations enables substantial subsurface  
73 flow, subsequently forming perennial water features such as warm springs. In spring, the soils which  
74 make up the active layer allow for rapid infiltration of meltwater, which laterally distributes  
75 nutrients and organic matter throughout the island's aquatic ecosystems (Westergaard-Nielsen et  
76 al., 2020). For example, during spring runoff meltwater and hillside topography was found to largely  
77 drive the distribution of nitrates from terrestrial to aquatic ecosystems (Zastruzny et al., 2017;  
78 Stevenson et al., 2021). Thus, pools of nutrients available during the growing season may vary  
79 dramatically from one year to the next. Lateral flow of snowmelt and permafrost thaw may influence  
80 CH<sub>4</sub> fluxes due to changes in physio- and biogeochemical properties of the lakes, streams and rivers  
81 on the island (Liebner et al., 2011; Rautio et al., 2011; Walvoord & Kurylyk, 2016; Stevenson et al.,  
82 2021). Although Disko Island has discontinuous permafrost (Christiansen et al., 2015; Kluge et al.,  
83 2021), thawing can release trapped organic matter and nutrients into aquatic ecosystems,  
84 potentially affecting CH<sub>4</sub> fluxes by providing new substrates for microbial activity (Ravn et al., 2020;  
85 Stevenson et al., 2021; Westergaard-Nielsen et al., 2020; Xu et al., 2021).

86 The distribution and drivers of aquatic CH<sub>4</sub> emissions in permafrost regions remain poorly  
87 constrained, particularly across small lakes and streams which may arise as emission hotspots.

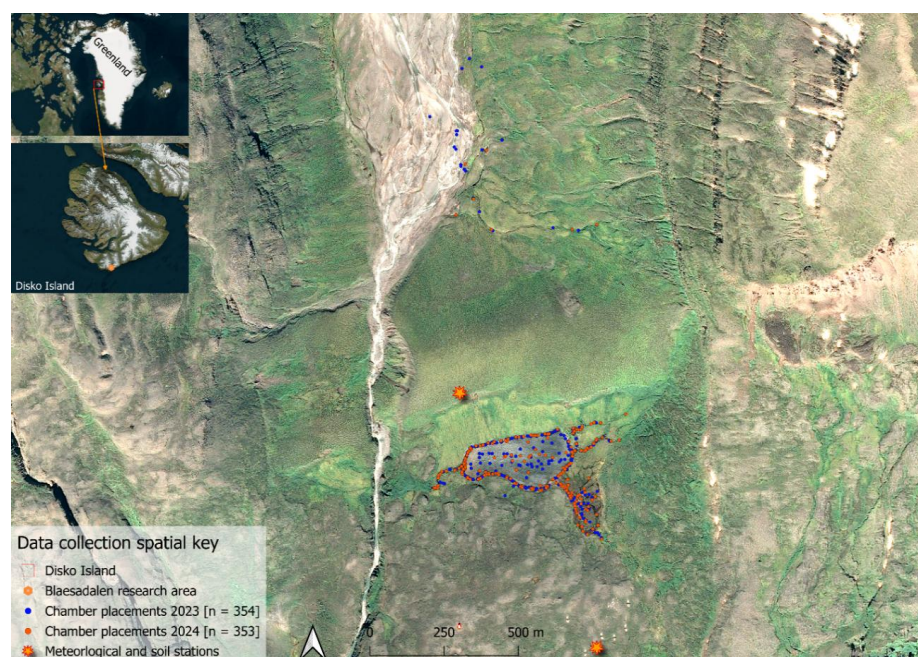


88 Previous studies on Disko Island have highlighted the potential importance of hydrology, permafrost  
 89 thaw, and microbial processes for greenhouse gas fluxes, but comprehensive spatial and seasonal  
 90 assessments of CH<sub>4</sub> are lacking. In this study we address this gap by quantifying CH<sub>4</sub> fluxes from 707  
 91 floating chamber measurements across a permafrost-affected catchment (Sanningasup Tasia). Using  
 92 boosted regression trees, we evaluate the partial effects of physiochemical water conditions,  
 93 catchment soil conditions, and meteorology in regulating emissions from ice-break through the  
 94 growing season. Our objective was to determine how spatial heterogeneity and seasonal dynamics  
 95 shape CH<sub>4</sub> emissions from Arctic freshwater ecosystems and to identify the key processes that  
 96 control flux variability in permafrost catchments.

## 97 2 Methods

### 98 2.1 Study Site

99 Lake Sanningasup Tasia in Greenlandic, or Moræne sø in Danish, is situated between  
 100 moraines in the north and east and an outlet which drains into the Red River to the west (Figure 1).  
 101 The lake is primarily fed by a large warm spring which enters the lake from the southeast, forming a  
 102 wetland type ecosystem. The other inlets of the lake are primarily fed by seasonal snowmelt. The  
 103 heterogeneity of the catchment provides an exemplary study site, allowing us to understand the  
 104 mechanisms regulating CH<sub>4</sub> emissions from a lake, streams, and wetland. According to a 2018 report  
 105 from the University of Copenhagen, the lake has a maximum depth of 4.5 m and is generally  
 106 phosphorus limited with nitrogen concentrations being seasonally variable, where concentrations  
 107 during ice cover are higher than during periods of no ice cover (Westergaard-Nielsen et al., 2020).  
 108 We found water temperature of the lake to range between 1.1 and 13.9 °C with a mean of 7.9 °C. To  
 109 our knowledge there has never been an extensive study on the greenhouse gas fluxes from the lake  
 110 and surrounding water bodies.



111  
 112 Figure 1. Map showing the 707 chamber measurements (blue and brown dots). Points in the south  
 113 are concentrated around Lake Sanningasup Tasia and its connected streams, while the points north



114 of the lake are measurements taken from the Red River and its stream tributaries. Orthomosaic  
 115 background image © CNES (2024), Distribution Airbus DS, produced from Pléiades 1B satellite  
 116 imagery.

## 117 2.2 Data Collection

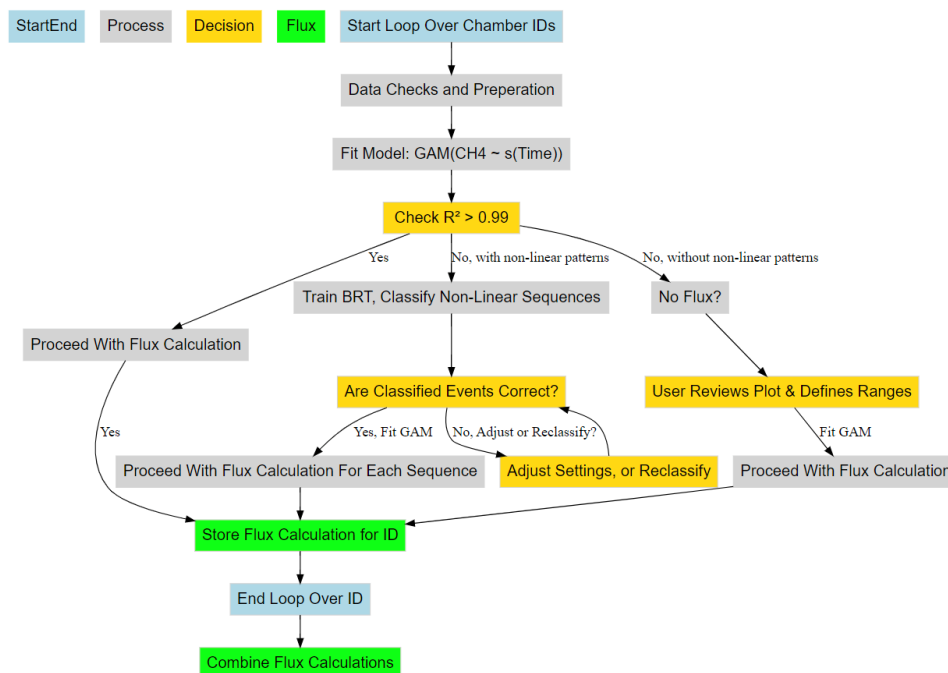
118 We used closed floating chamber systems connected to an ABB/Los Gatos Research GLA131  
 119 Series Micro portable Gas Analyzer in 2023, and to a LI-COR® LI-7810 Trace Gas Analyzer in 2024,  
 120 with the goal of capturing the spatial and temporal variability of CH<sub>4</sub> fluxes in the catchment area. In  
 121 2023, we used a self-built cylindrical chamber made of semi-transparent plastic material with  
 122 volumetric capacity of 0.016 m<sup>3</sup> and a basal area of 0.096 m<sup>2</sup>. In 2024, we used a West Systems type  
 123 C flux chamber made of stainless steel with a volumetric capacity of 0.013 m<sup>3</sup> and a basal area of  
 124 0.07 m<sup>2</sup>. Both chambers included a fan for mixing air and a temperature sensor. Chamber  
 125 measurements were conducted on the surface of the lake and surrounding water bodies at a spatial  
 126 distance of 10 to 20 m with a closure time of 10 minutes. The chamber and gas analyzer were  
 127 connected in a closed loop, and sample air was continuously pumped through the gas analyzer. CH<sub>4</sub>  
 128 concentrations were measured with a frequency of 1 Hz. Each flux measurement was given a unique  
 129 id based on its spatial location or water body type. For the lake, ids were given based on what  
 130 shoreline we were measuring on. For example, if on the east shore, ids would be e1, e2, e3, ... etc.  
 131 The majority of flux measurements on the lake were conducted within 0.2 m from the shore. Open  
 132 water measurements in the lake were made using a small boat and anchor system. CH<sub>4</sub>  
 133 concentrations in streams were measured by starting at, or near the headwaters and then taking  
 134 measurements progressively downstream with consideration to the changing terrestrial vegetation  
 135 and stream dynamics (i.e., fast, slow, or eddie pool). In 2023 meltwater pools during the thaw  
 136 season were measured to capture control conditions, or water distinct from that which is in the lake  
 137 and streams. However, in 2024 we took measurements on top of snow and ice to capture a control  
 138 period before thaw season took hold in the catchment. Overall, we made 707 chamber  
 139 measurements around the lake and surrounding streams giving us an extensive view of the spatial  
 140 and temporal variability of CH<sub>4</sub> fluxes in the study area. We simultaneously measured water  
 141 temperature using Truebner EC-100 RS-485 EC/Temperature sensors in 2023 and a suite of water  
 142 parameters were collected in 2024 using an AquaTroll 600 water sonde (see section: Decoding  
 143 Methane Drivers). Meteorological data and soil characteristics were collected from nearby  
 144 meteorological stations maintained by Aarhus University which are part of the Greenland Ecosystem  
 145 Monitoring Database (Greenland Ecosystem Monitoring, 2025a-d) (see section “Decoding Methane  
 146 Drivers” for list of variables used).

## 147 2.3 Flux Algorithm & Ebullition Detection

148 In collaboration with ChatGPT 4.0, we wrote an interactive algorithm in R which leverages  
 149 General Additive Models (GAM) and Boosted Regression Trees (BRT) to robustly and flexibly  
 150 calculate CH<sub>4</sub> fluxes from individual floating chamber measurements (Figure 2).



151



152

153 Figure 2. CH<sub>4</sub> flux calculation workflow from concentration data using predictions from GAM and  
 154 BRT. Blue boxes represent the start and end of a single chamber measurement working through the  
 155 algorithms processes (grey boxes) and decision logic (gold boxes). Green boxes represent the storage  
 156 and combination of the results for further analysis.

157 Rather than fitting concentration data with linear, exponential, and/or polynomial models  
 158 (Kutzbach et al., 2007; Pedersen et al., 2010; Hoffmann et al., 2017), the algorithm fits GAM, which  
 159 are capable of modelling non-linear patterns without a-priori specification of the functional form of  
 160 the relationship between time and concentration. However, before fitting a GAM, the concentration  
 161 and accompanying data is checked and processed (Figure 2; “Data Checks and Preparation”) as  
 162 follows: The algorithm conducts a preliminary check for the required chamber parameters which  
 163 are; id, ordered times of measurement, air temperature (°C), volume, area, and air pressure. In  
 164 addition, air temperature is expected to be initially in Celsius, which is automatically converted to  
 165 Kelvin during the processing of concentration data in preceding steps. The data is then ordered  
 166 based on id and time to maintain correct chronological order of chamber measurements. CH<sub>4</sub> is then  
 167 converted from ppm to moles using Ideal Gas Law:

168

$$169 \quad CH_4_{moles} = \frac{(CH_4 ppm \times P \times V)}{(R \times T)} \quad (1)$$

170

171 where P is air pressure (Pa), V is chamber volume (m<sup>3</sup>), R (8.314 J/ (mol × K) is the universal gas  
 172 constant, and T is air temperature inside the chamber (K). After preliminary data checks and initial





processing of the concentration data, the data is then fit to a GAM (i.e.  $\text{gam}(\text{CH}_4_{\text{moles}} \sim s(\text{time}, k = \text{gam\_knots}))$ , where the smoothing parameter 'k' is a user defined parameter named 'gam\_knots' which has a default value of 5. The value of 'k' cannot exceed 3 times the degrees of freedom for a given concentration time series, or the algorithm defaults to fitting a linear model. The algorithm then checks the  $R^2$  value of the fitted GAM to see if it meets the default conditional value of  $\geq 0.99$ , if so, it proceeds to calculate fluxes following these steps:

179

$$\Delta \text{CH}_4_{\text{moles}} = \left[ \frac{\text{CH}_4(t_2) - \text{CH}_4(t_1)}{t_2 - t_1}, \frac{\text{CH}_4(t_3) - \text{CH}_4(t_2)}{t_3 - t_2}, \dots, \frac{\text{CH}_4(t_n) - \text{CH}_4(t_{n-1})}{t_n - t_{n-1}} \right] \quad (2)$$

181

Where  $\Delta \text{CH}_4_{\text{moles}}$  is the rate of change, calculated as the quotient of the predicted differences in  $\text{CH}_4$  concentration between successive time points. Flux is then calculated between successive time points by:

185

$$\bar{F}_{\text{Flux}} = \frac{1}{n-1} \sum_{i=1}^{n-1} \frac{\Delta \text{CH}_4}{A} \quad (3)$$

187

Where mean flux of the chamber measurement is estimated by calculating flux at each successive time step, where flux is determined by dividing  $\Delta \text{CH}_4_{\text{moles}}$  by the basal area (A) of the chamber, expressed in ( $\text{m}^2$ ). A plot of the time series and model fit is generated and saved in the file directory defined by the user by setting the parameter 'save\_directory' (Figures S1-5). In the cases where the initial GAM fit does not meet the  $R^2 \geq 0.99$  condition, the algorithm can follow two pathways (Figure 2). Pathway (1) is a result of the algorithm having detected non-linear concentration increases using BRT, while pathway (2) the algorithm has found the chamber measurement has not met any of the conditional requirements for flux calculations, or more generally stated, there was no measurable concentration increase detected automatically. Both pathways are interactive as the user is prompted to confirm the classification of "ebullition" v. diffusive data sequences in pathway (1), while in pathway (2) the user confirms there is indeed no concentration increase by reviewing the diagnostic plot (see Supplemental text). Once confirmed, the user initiates flux calculations by manually entering the time range of the measurement that should be fitted (Figure 2).

## 202 2.5 Lake and Stream Metabolism

In 2024, we calculated the metabolic parameters net ecosystem production (NEP), gross primary production (GPP), and ecosystem respiration (ER) of oxygen for the lake and streams using high-frequency dissolved oxygen (DO) collected at a one-minute frequency during chamber measurements. Including metabolic parameters as predictors in the BRT models gave us an understanding of the role microbial oxygen production plays in regulating or not  $\text{CH}_4$  emissions from water. DO saturation was adjusted using temperature-dependent solubility constants (Garcia & Gordon, 1992). Oxygen flux at the air-water interface was determined using wind derived gas exchange coefficients and adjusted for water temperature (Cole & Caraco, 1998). NEP was calculated as the rate of change in DO concentration over each chamber deployment, adjusted for air-water exchange. GPP and ER were partitioned from NEP by applying a threshold of  $200 \mu\text{mol m}^{-2} \text{s}^{-1}$  photosynthetically active radiation (PAR), which distinguishes intervals with effective photosynthesis from those with negligible light-driven production, despite continuous daylight



215 during Arctic summer. Aggregating each chamber measurement into one-minute intervals, we  
 216 calculated mean NEP, GPP, and ER for each chamber placement (Winslow et al., 2016). While this  
 217 methodology is sound for the lake, there is some caveats in relation to stream metabolism. Because  
 218 we are using a model which assumes wind driven gas exchange for small streams, we likely  
 219 underestimate gas exchange in parts of the streams where turbulence from streambed roughness  
 220 dominates. Nonetheless, the approach captures broadly the trends in stream metabolism and is  
 221 useful for comparing fluxes across aquatic biomes (Mulholland et al., 2001; Hall & Madinger, 2018;  
 222 Noss et al., 2018).

## 223 2.4 Spatial Flux Evaluation

224 We uploaded as a spatial layer in QGIS version 3.40.1 (QGIS Development Team, 2025) an  
 225 orthomosaic image produced by Airbus satellite Pléiades 1B and the chamber placements as points  
 226 with their associated flux estimates. We spatially analyzed the CH<sub>4</sub> fluxes by creating bi-weekly  
 227 emission heatmaps using the Kernel Density Estimation (KDE) algorithm in QGIS. We set the radius to  
 228 between 30-35 meters to allow some connectivity between points which allows for a smooth  
 229 representation of any environmental gradients that might be captured. We used the default method  
 230 using a quartic kernel shape weighted by the flux calculated for each chamber placement. While  
 231 ebullitive fluxes were not considered in further statistical analysis (i.e., in the BRT), those fluxes are  
 232 depicted in the resulting heatmaps. Overall, using KDE allowed for an intuitive interpretation of the  
 233 seasonal and spatial development of flux hotspots in the research area.

234 We additionally compared daily CH<sub>4</sub> emissions from Sanningasup Tasia catchment relative to  
 235 other Arctic-Boreal Lake classes compiled in the Boreal-Arctic Wetland and Lake Dataset (Kuhn et al.  
 236 2021; Olefeldt et al., 2021). A Kurskal-Wallis test was performed to determine significant differences  
 237 ( $p < 0.05$ ) in the log transformed daily fluxes from Sanningasup Tasia ( $n = 48$ ) and its streams ( $n = 35$ )  
 238 relative to broader biome-scale fluxes from Small Peat Lakes ( $n = 50$ ), Medium Peat Lakes ( $n = 36$ ),  
 239 Large Lakes ( $n = 10$ ), and Small Yedoma Lakes ( $n = 7$ ). We then performed pairwise Wilcoxon rank-  
 240 sum tests with Benjamini-Hochberg adjustment for multiple comparisons to highlight specific  
 241 contrasts between Sanningasup Tasia catchment and the other lake classes. Conducting this  
 242 provides an understanding of how Sanningasup Tasia catchment emissions compares to other Arctic  
 243 waterbody types.

## 244 2.6 Decoding Methane Drivers

245 To determine important drivers and their partial effects on diffusive CH<sub>4</sub> fluxes, we trained  
 246 BRT with physicochemical water parameters, soil temperatures, soil moisture, surface air  
 247 temperatures, local meteorology, and Julian day (Figure 3). We have focused on diffusive fluxes due  
 248 to the unpredictability of fluxes when ebullitive processes were considered in the models. The  
 249 diffusive fluxes give us a detailed view of environmental controls shaping CH<sub>4</sub> fluxes coming from the  
 250 catchment. Conductivity ( $\mu\text{S}/\text{cm}$ ), pH, redox potential (mV), dissolved oxygen (mg/L), oxygen  
 251 saturation (%), water temperature ( $^{\circ}\text{C}$ ), and fluorescent dissolved organic matter (FDOM; RFU), were  
 252 included in the models to capture the influence of physicochemical water properties on CH<sub>4</sub> fluxes  
 253 from the lake and streams (Figure S6). Lake water levels (mm) were included to characterize the  
 254 effect of changing hydrologic conditions and its influence on lake CH<sub>4</sub> fluxes. Soil characteristics were  
 255 included to capture the hydrogeological conditions surrounding the catchment. Soil temperatures  
 256 ( $^{\circ}\text{C}$ ), at 40 cm were included in the models to gain an understanding of whether or not the  
 257 catchment soil conditions influence surface water CH<sub>4</sub> fluxes. Soil volumetric water content (VWC) at  
 258 10 cm was included to gain an understanding if dryer, or wetter soil conditions effect surface water  
 259 CH<sub>4</sub> fluxes, and to act as a substitute for water level in the lake early in the season as these two  
 260 share a Pearson's correlation of  $r = 0.93$ . Surface air temperature at 2 cm ( $^{\circ}\text{C}$ ), Air temperature ( $^{\circ}\text{C}$ ),



261 relative humidity (%), air pressure (mbar), precipitation (mm), PAR ( $\mu\text{mol}/\text{m}^2/\text{s}$ ), and mean wind  
262 speed ( $\text{m s}^{-1}$ ) and direction ( $^\circ$ ) were included in the models to characterize the influence of near  
263 surface freeze conditions and local meteorology on  $\text{CH}_4$  fluxes from the catchment area,  
264 respectively. To reduce multicollinearity amongst the predictors, we set up weighting for random  
265 feature selection by calculating the average absolute Pearson correlations between predictors and  
266 assigning weights inversely proportional to the correlations, resulting in higher weights given to  
267 predictors with decreased collinearity and thus more likely to be included as a predictor.

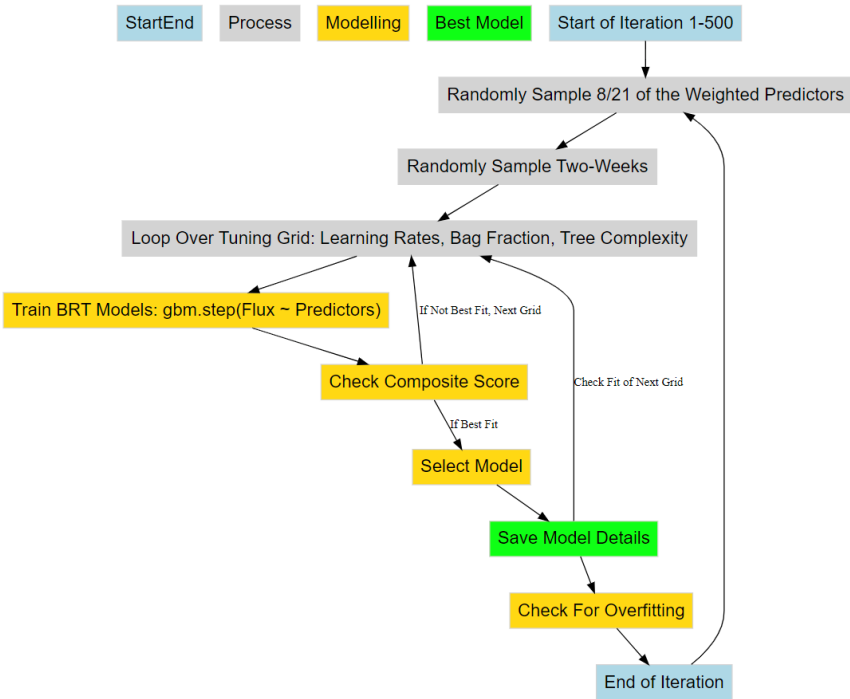
268 Using the “gbm.step” algorithm from the R package “dismo” version 1.3.14 (Elith et al.,  
269 2008; Hijmans et al. 2023), we iteratively attempted to fit 500 BRT with a subset of randomly  
270 sampled two-week time series of flux calculations and 7 of the 21 weighted predictors. Each two  
271 weeks must have at least 90 observations, or the date range is buffered on either end of the time  
272 series to meet the minimum observation requirement. The algorithm uses 10-fold cross-validation to  
273 minimize overfitting the models (Elith et al., 2008). If a randomly sampled two weeks did not meet  
274 the minimum required observation of 90, the time series was buffered on both ends of the date  
275 range to meet the minimum required observations. BRT were optimized using a grid search where  
276 hyperparameters such as learning rate (0.001, 0.002, 0.003, 0.004, 0.005), tree complexity (1, 3, 5,  
277 7), and bag fraction (0.30, 0.40, 0.50), were tuned for each model fit. Variable monotonicity was  
278 handled dynamically for each subset of predictors using Spearman’s rank correlation. Monotonicity  
279 for categorical variables was set to zero, while positive correlations were given a +1 and negative  
280 correlations were given a -1. The model with the best composite score was selected for each  
281 iteration. The composite score was calculated by adding together the standardized cross-validation  
282 error, standardized correlation error, and the cross-validation correlation. The model was finally  
283 saved after checking for over fitting by taking the difference between cross validated mean deviance  
284 and training mean deviance and dividing the difference by training mean deviance. Because the  
285 inherently noisy nature of ecological data, we allowed for 40% difference between cross validated  
286 predictions and training data. We further calculate the overall deviance explained across the  
287 successfully fitted models. Each fitted model and its metadata were saved for further analysis. This  
288 modelling structure ensures robustness against outliers and ensures data integrity through  
289 dynamically handling monotonicity and applying overfitting constraints. Furthermore, the structure  
290 ensures robust predictions of fluxes by accounting for multi-collinearity amongst predictors and flux  
291 heterogeneity throughout the season.

292 To visualize the results of the models, we plotted partial dependence two ways. First, we  
293 extracted partial dependence information for understanding model structure, i.e., those predictors  
294 and interactions which were used to split trees and decrease cross validated prediction error. In  
295 addition, we made isolated predictions for each environmental feature in the model by holding all  
296 other predictors at their median to gain a more mechanistic understanding of which conditions  
297 and/or processes are directly affecting  $\text{CH}_4$  fluxes. The two ways of visualizing partial dependence  
298 give us an ecological understanding of how integrated direct and indirect effects regulate fluxes from  
299 the catchment, but also how individual variables and/or processes regulate fluxes from the water  
300 surfaces, respectively. All visualizations were generated using the R package “ggplot2” version 3.5.0  
301 (Wickham, 2016), and the package “DiagrammeR” version 1.0.11 for flowcharts (Iannone, 2024).





302



303

304 Figure 3. Workflow of the iterative randomized process for selecting the best BRT for predicting  
305 diffusive CH<sub>4</sub> fluxes using various environmental predictors. Blue boxes represent the start and end  
306 of a single iteration through an index of weighted predictors, time periods, and tuning grid (grey  
307 boxes). Yellow boxes represent the model selection logic, while the green box represents the storage  
308 of flux predictions and selected model details for the included predictors and two-week sub-sample  
309 of chamber measurements.

### 310 3 Results and Discussion

#### 311 3.1 Overview

312 Methane fluxes from permafrost affected catchments are influenced by a complex interplay  
313 between climatological, hydrogeological, and biogeochemical processes. This study highlights the  
314 transient nature of CH<sub>4</sub> fluxes from a permafrost catchment in west central Greenland and the  
315 partial effects of physiochemical water conditions, local meteorology and catchment conditions  
316 (Figures 4-7). CH<sub>4</sub> emissions from the catchment were variable across water conditions, with streams  
317 exhibiting the highest emissions (Figure 4). In comparison to the global coverage of the Boreal-Arctic  
318 Wetland and Lake Dataset (Olefeldt et al., 2021), besides small peat lakes, daily fluxes from  
319 Sanningasup Tasia at 8.3 mg m<sup>-2</sup> d<sup>-1</sup> were mostly comparable to other permafrost waterbodies across  
320 the Arctic-Boreal region, which ranges between 3.8-5.4 mg m<sup>-2</sup> d<sup>-1</sup> (Figure 4). Highlighting the  
321 importance of emissions from small streams, Sanningasup Tasia streams showed significantly higher  
322 daily fluxes (18.2 mg m<sup>-2</sup> d<sup>-1</sup>) than all inland water body classes, except Yedomal lakes (43.7 mg m<sup>-2</sup> d<sup>-1</sup>).  
323 Our results indicate that CH<sub>4</sub> fluxes were seasonally variable and controls on fluxes shifted from  
324 hydroclimatic factors during colder periods to biogeochemical processes as the catchment warmed



and increased in productivity (Figure 3-4 and Figure A1). The seasonal thaw of annual snow and ice accumulation in the two study years varied in timing and duration due to 2023 staying anomalously snowy until the beginning of July, where in 2024 the number of snow free days aligned with historical records. In 2023, our initial chamber measurements between July 03-15 captured peak median fluxes at  $8.9 \text{ nmol m}^{-2}\text{s}^{-1}$  just as the ice began to break on the lake. In an effort to capture similar conditions in 2024, we used an index of historical snow free days on the island which led to us capturing median fluxes of  $0.18 \text{ nmol m}^{-2}\text{s}^{-1}$  between May 24-June 05 atop ice and snow. Peak median fluxes of  $8.1 \text{ nmol m}^{-2}\text{s}^{-1}$  in 2024, were comparable to 2023, but occurred a month earlier between June 11-19. As runoff water receded and the catchment warmed, growing season commenced in conjunction with steadily decreasing median fluxes between  $3.9$  and  $4.5 \text{ nmol m}^{-2}\text{s}^{-1}$ . The use of KDE allowed us to smooth across discrete chamber measurements, yielding an intuitive continuous surface representation of  $\text{CH}_4$  flux hotspots and their evolution through time (Figure 2). This study further provides methods to disentangle important drivers and their partial effects on  $\text{CH}_4$  fluxes using BRT (Figure 3-4). In general,  $\text{CH}_4$  fluxes were strongly dependent on discrete oxic-anoxic aquatic environments under the chamber (Figure 4 and Figure A1). This research emphasizes the importance of integrating field measurements with GIS-based spatial analysis to monitor  $\text{CH}_4$  fluxes in permafrost catchments. It further drives home the importance of seasonal transition periods in predicting fluxes from Arctic waterbodies.

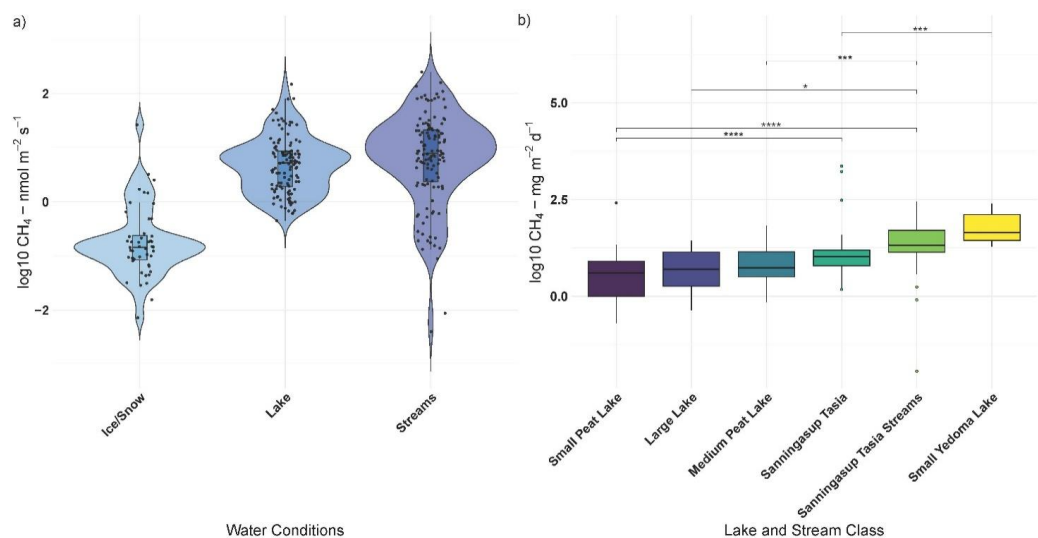


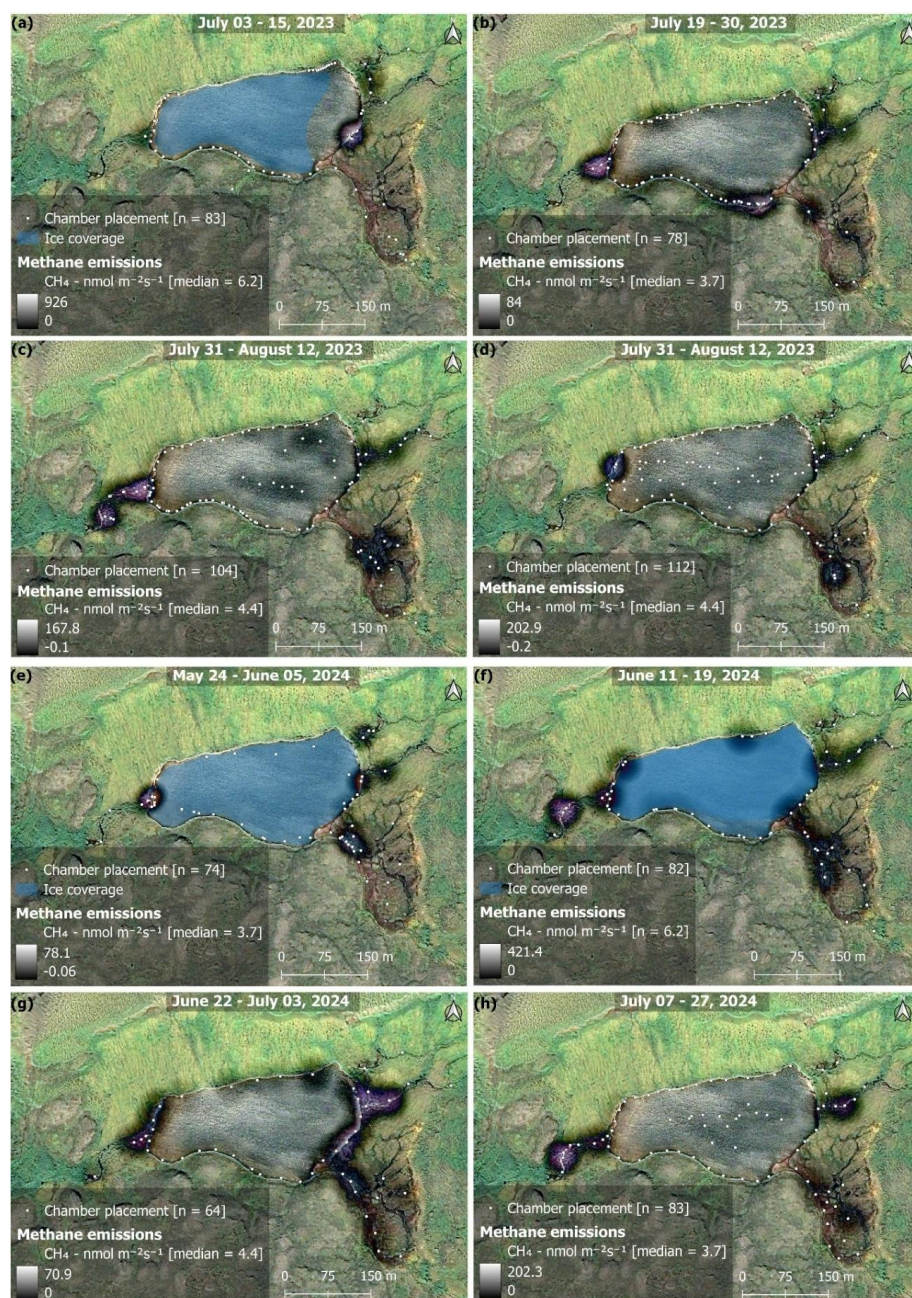
Figure 4. Panel a) shows log transformed  $\text{CH}_4$  fluxes across the different catchment water conditions during 2024 field season and b) compares log transformed daily  $\text{CH}_4$  fluxes (y axis) between Sanningasup Tasia catchment and other permafrost waterbodies (Kuhn et al., 2021) across the Arctic-boreal region. Connecting brackets and stars show, for example, that Sanningasup Tasia had significantly ( $p < 0.05$ ) higher daily emissions when compared to Small Peat Lakes, while daily emissions from Sanningasup Tasia Streams were significantly higher than all lake classes except Yedoma Lakes.

### 3.2 Spatial and Temporal Evolution of Methane Fluxes

In both 2023 and 2024, spatial and temporal evolution of fluxes occurred somewhat heterogeneously in the catchment, but generally “hotspots” occurred in the streams and where they enter the lake (Figure 5 a-b, e-f). Despite different time periods of the thaw, fluxes in the catchment



355 in both years followed a similar trajectory, with peak fluxes occurring post thaw and decreasing  
356 through the growing season. In 2023, snow persisted anomalously late into the summer season, and  
357 soil temperatures were the coldest recorded in a 6-year record (Figure S7). We found that local  
358 climate and catchment soil characteristics were at times, (i.e., during the thaw season and towards  
359 the peak of growing season) more important than water temperature in predicting 2023 fluxes,  
360 suggesting catchment contributions to surface waters plays an indirect role in CH<sub>4</sub> fluxes (Figure S8).  
361 While water temperature was found to be relatively important in both years, catchment CH<sub>4</sub> fluxes in  
362 2024 suggest the system is more driven by variability in dissolved organic matter and microbial  
363 production of oxygen (Figure 4-7 and Figure A1).



364

365 Figure 5. Maps showing the bi-weekly spatial evolution of  $\text{CH}_4$  emissions during 2023 (a-d) and 2024  
 366 (e-h). The time period covered in each map is given at the top of each map. Whiter colors represent  
 367 areas of high emissions, while darker, or no color represent areas of lower, or no emissions (see  
 368 color bars in map legends). Areas outside of the water were not measured and are artifacts from the  
 369 KDE mapping algorithm. Each white point on the map represents the placement of the floating





370 chamber. Orthomosaic background image © CNES (2024), Distribution Airbus DS, produced from  
 371 Pléiades 1B satellite imagery.

372 The main inlet to the lake is a warm spring with median temperatures of 7.4 °C and tended  
 373 to be a persistent location throughout the season for increased CH<sub>4</sub> fluxes. The warm spring area in  
 374 the southeast is a complex area where a perennial spring bubbles out of the ground forming a  
 375 perennial tributary to the lake. However, the spring seeps out along the base of the hillslope to the  
 376 east, subsequently forming a peat fen environment (Figure 5). The eastern most inlets are fed by  
 377 meltwater flowing through the vadose zone, but also served as a persistent location for increased  
 378 CH<sub>4</sub> fluxes. Fluxes from inlet streams followed along an upland-wetland environmental gradient,  
 379 where fluxes at the headwaters of streams were generally close to 0, or slightly taking up CH<sub>4</sub>, but  
 380 steadily increased as steeper upland slopes gave way to more gradual water saturated slopes and  
 381 pooling sediments. This is consistent with previous work on the island showing CH<sub>4</sub> fluxes association  
 382 with soil microbial assemblages shifting from methanotrophic to methanogenic along an upland-  
 383 wetland gradient, respectively (Christiansen et al., 2015). Additionally, the catchment serves as  
 384 micro-topography previously described as an area of snowmelt retention, and subsequently an area  
 385 of nutrient and/or dissolved organic matter pooling (Westergaard-Nielsen et al., 2020), which has an  
 386 impact on CH<sub>4</sub> fluxes throughout the season (Figure 7). While high fluxes were recorded along the  
 387 shore and in the open water of the lake, fluxes tended to be patchy and decreased moving away  
 388 from the inlet streams (Figure 5). However, as soon as the lake water flowed to the outlet, fluxes  
 389 increased substantially. Fluxes dissipated through the season until fluxes were isolated to the warm  
 390 spring inlet and the eastern inlets (Figure 5). Field observations of late-season fluxes in 2024, found  
 391 decreased fluxes were associated with submerged filamentous green algae in stream channels, while  
 392 assemblages of iron-oxidizing bacteria on the stream banks were associated with increased fluxes,  
 393 (Figure A2). The spatial and temporal evolution of fluxes was driven by seasonally shifting  
 394 environmental conditions.

### 395 3.3 Boosted Regression Tree Results

396 Out of 500 iterations, 321 BRT were fit, and showed good alignment and consistently  
 397 performed well in cross-validation, with a correlation median of 0.40 between observed and  
 398 predicted values, and a median deviance standard error of 131. Between 8.4% and 62.4% with a  
 399 median of 27.3% of the CH<sub>4</sub> flux variability was explained by the various models and included  
 400 environmental conditions, suggesting a substantial proportion of CH<sub>4</sub> fluxes were explained by the  
 401 environmental conditions included. The calculated root mean squared error (RMSE), which reflects  
 402 the average magnitude in prediction error of the BRT, ranged between 6.5 to 28 nmol m<sup>-2</sup>s<sup>-1</sup>, with a  
 403 median of 13.7 nmol m<sup>-2</sup>s<sup>-1</sup>. The summary statistics reflect models that performed reliably and with  
 404 fairly good accuracy in predicting diffusive CH<sub>4</sub> fluxes from the catchment in 2024. The models  
 405 predicted shifting relative importance (Figure 6) and partial effects of the various environmental  
 406 conditions throughout the season (Figure 7). The magnitude of CH<sub>4</sub> fluxes predicted by the BRT  
 407 models were strongly influenced by localized biogeochemical conditions within the water column  
 408 based on whether the flux was originating from the lake, stream, or if it was influenced by ice or  
 409 snow (Figure 4-7, and Figure A1a-d). Visualizing partial dependence of predictors important for  
 410 model structure, revealed integrated ecological effects between local meteorology, catchment  
 411 conditions and physiochemical water conditions (Figure 7). However, isolated direct marginal effects  
 412 of the various environmental conditions suggest fluxes from water surfaces are directly regulated via  
 413 biochemical processes associated with GPP and ER of oxygen (Figure A1b-d).



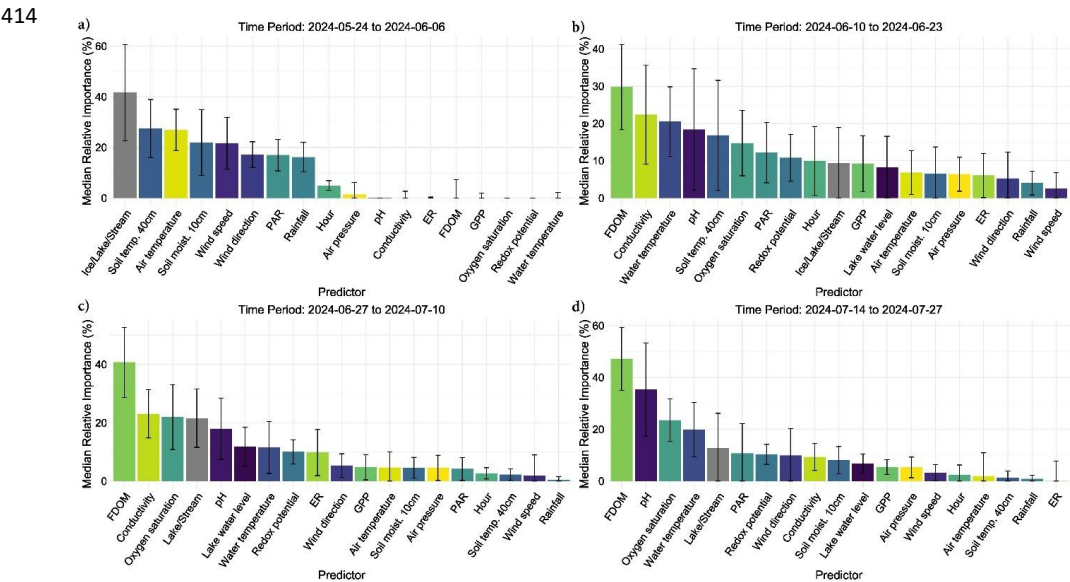
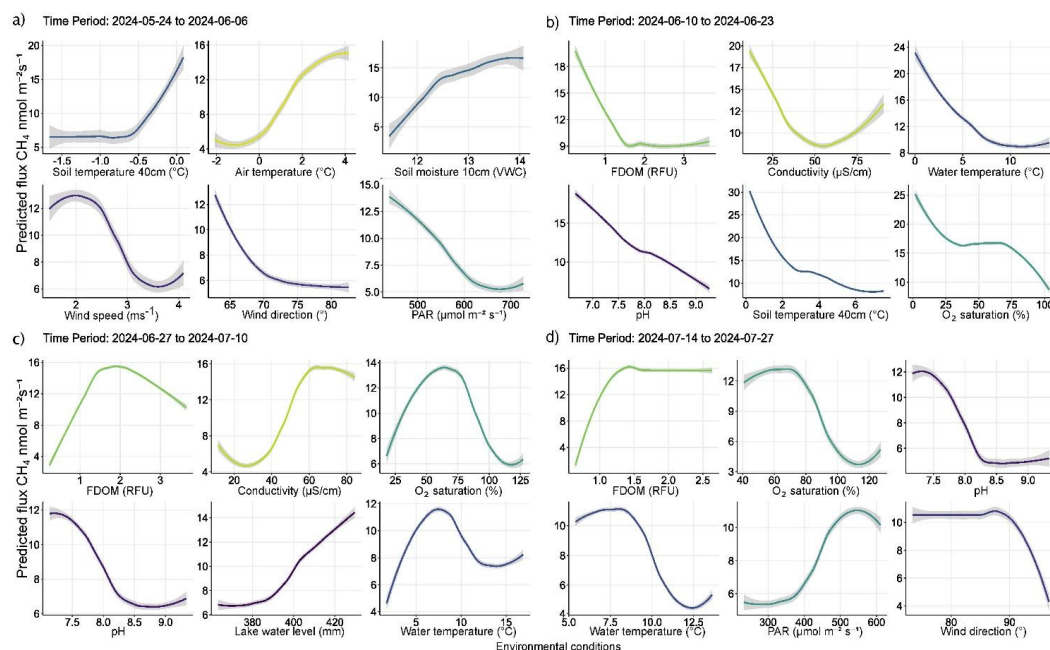


Figure 6. The figure illustrates the relative importance of environmental conditions predicting diffusive CH<sub>4</sub> fluxes using bar-plots and standard error bars. Each predictor variable is on the x-axis, while its percent importance for its inclusion in a fitted BRT is given on the y-axis where the standard error bars represent variability in importance based on presence or absence in a given model. Each bar color represents a distinct environmental condition.

### 3.3.1 Spring Thaw Phase: Peak Fluxes Driven by Hydrological and Climatic Controls

The spring thaw phase marks a shift in catchment conditions, where a frozen landscape gives way to thaw season and hydro-connectivity between land and water is strong (Figure 5c-d, g-h). In the spring thaw phase, initial peak fluxes of CH<sub>4</sub> were primarily dependent on increasing rainfall, changing wind conditions, warming air and soil temperatures, and increased soil moisture content, while low dissolved organic matter (i.e., FDOM) indicated increased fluxes (Figure 6a-b and 7a-b). Soil moisture was found to have a Pearson's  $r = 0.93$  with lake water levels, suggesting the lake levels are strongly connected to snowmelt and groundwater hydrology (Figure S9). The distribution of nutrients, i.e., dissolved organic matter (DOM), on the island has been shown to be linked to snowmelt and hill slope topography (Westergaard-Nielsen et al., 2020), which is likely playing a role during the early part of the season, but especially later in the year as DOM becomes the primary limiting factor in predicting higher fluxes (Figure 7b-c) (Olid et al., 2021, 2022). The processes driving CH<sub>4</sub> fluxes from water surfaces is likely two-fold.



434

435 Figure 7. Partial dependency plots illustrating the indirect and direct marginal effects of various  
 436 environmental conditions predicting diffusive CH<sub>4</sub> fluxes. Each panel displays the effect of a  
 437 numerical predictor used during model training to predict CH<sub>4</sub> fluxes. Although some predictors may  
 438 not have been directly involved in regulating fluxes from water surfaces, their evaluation reveals the  
 439 relationship between water column conditions and catchment processes regulating CH<sub>4</sub> fluxes. The  
 440 figures are ordered by importance in each time period and the colors correspond to those seen in  
 441 Figure 6. The colored lines represent the result of a fitted general additive model ( $y \sim s(x)$ ) and thus  
 442 a smooth representation across the 321 fitted BRT models. Each predictor and its numerical range  
 443 are given on the x-axis, while predicted fluxes are given on the y-axis.

444 As snowfall turned to rain, the thawing of soils accelerated and water content in the active  
 445 layer increased, potentially driving peak emissions via the lateral mobilization of dissolved CH<sub>4</sub>  
 446 toward surface waters (Figure 7a-b) (Walter Anthony et al., 2012; Neumann et al., 2019; Olid et al.,  
 447 2022). However, as the thaw progressed, contributions to fluxes from catchment soils decreased as  
 448 the upper layers began to dry and lake water levels reached their maximum (Figure 7b-c). DOM  
 449 serves as a critical substrate for both CH<sub>4</sub> production and oxidation, particularly in permafrost-  
 450 influenced regions where thawing can release large amounts of particulate matter (Keskitalo et al.,  
 451 2021; Bouranis et al. 2025). Anaerobic conditions in water saturated soils and low oxygenated  
 452 waters may have further driven fluxes during the thaw period as methanogenic microbial  
 453 communities rapidly consumed incoming labile organic compounds (Neumann et al., 2019;  
 454 Stevenson et al., 2021). However, as the thaw progressed, the lake briefly shifted to net-autotrophy  
 455 (Figure S6), marking an important shift from hydroclimatic controls on fluxes, to a patchwork of  
 456 biochemical transport pathways and barriers (Figure 7 b-d and Figure A1b-d). During this transition,  
 457 increased GPP and the resulting oxygen saturation in the lake and streams enhance methanotrophic  
 458 activity, thereby promoting methane oxidation and reducing net CH<sub>4</sub> emissions (Figure 7b-c and  
 459 Figure A1b-c). The central role of oxygen availability and active methanotroph communities in  
 460 regulating methane fluxes during Arctic thaw has been demonstrated in both tundra landscapes and



permafrost mires (Christiansen et al., 2015; Graef et al., 2011; Singleton et al., 2018). As oxygen production increases, greater amounts of oxygen become available to support methanotrophic activity in the water column. Methanotrophic activity is likely represented in the observed reduction of CH<sub>4</sub> fluxes during periods of decreased ER (i.e., when oxygen consumption is elevated, Figure A1c), as higher oxygen availability enhances aerobic methane oxidation (Figure 7c). However, the streams remain net heterotrophic despite increasing GPP and ER during this time period, therefore providing a more suitable environment for CH<sub>4</sub> production and flux (Figure S6). Thus, the lake and streams reflect distinct ecosystems for the production and flux of CH<sub>4</sub>, where the lake being an overall methane source, has a greater tendency to oxidize CH<sub>4</sub> following the thaw, while the streams follow along a low-to-high flux gradient as the slope flattens and soils become saturated (Westergaard-Nielsen et al., 2020; Stevenson et al., 2021).

### 3.3.2 Growing Season: Oxic-Anoxic Transport Pathways and Barriers

Early in the growing season the lake and streams enter into a transition phase, where peak fluxes become increasingly dependent on biochemical pathways related to DOM availability, conductivity, oxygen saturation and pH (Figure 7c). DOM is the limiting factor late in the season where higher fluxes are increasingly dependent on water column conditions with greater levels of DOM (Figure 6c-d and 7c-d). CH<sub>4</sub> fluxes during this time period were strongly associated with indicators of microbial activity forming oxic-anoxic transport barriers, or pathways, respectively. For example, microbial activity in anoxic sediments maybe producing CH<sub>4</sub>, but whether it is diffused to the atmosphere is directly affected by the micro-conditions of the water column (e.g., DOM, conductivity, pH, and/or GPP/oxygen saturation), either forming an oxidative barrier, or an anoxic pathway (Figure 7c-d and Figure A1). For example, groundwater transport of CH<sub>4</sub> from anoxic sediments to oxygen-rich streams may result in water with high concentrations of both. While some of the CH<sub>4</sub> is likely oxidized during transport, it can be that both are respired at turbulent sections of the stream, which were the highest fluxes observed from the streams and during this phase of the season (Street et al., 2016; Neumann et al., 2019; Olid et al., 2022; Kleber et al. 2025).

Fluxes are further affected by water conditions either favoring methanogenic, or methanotrophic activity (Conrad, 2007; Cunada et al., 2021; Emerson et al., 2021). pH levels near neutral likely indicate water conditions favorable to methanogenesis at the sediment-water interface, while increasing alkalinity may reduce methanogenic and/or favor increased methanotrophic activity as growing season progresses (Figure 7c-d). For example, during growing season micro-pH and oxygen saturation conditions in the lake and streams are influenced by the ever-increasing presence of macrophytes, mosses and plankton, which tend to drive pH and oxygen levels higher (Liebner et al., 2011; Cunada et al., 2021). Here we show, that increasing pH and oxygen saturation as a result of primary production drive CH<sub>4</sub> emissions down through the growing season (Figure 7c-d and Figure A1). Declines in oxygen saturation driven by microbial respiration can create anoxic conditions that enable CH<sub>4</sub> emissions from sediment to surface waters (Conrad, 2007; Michel et al., 2010; Street et al., 2016; Cheng et al. 2024). Such a mechanism likely explains the formation of flux hotspots associated with decomposing iron-oxidizing bacterial mats along stream banks (Figure A2) (Wallenius et al., 2021; Cheng et al. 2024). In the case of the bacterial mats, we observed fluxes were highest in the streams where bacterial assemblages had become exposed to the atmosphere and were decomposing in stagnant water (Figure A2), which may suggest that the decomposition of the bacteria was releasing dissolved organic substrates in a low-oxygen environment already primed for methanogenic activity (Wallenius et al., 2021; Cheng et al. 2024). This idea is supported late in the season when increased CH<sub>4</sub> emissions become dependent on niche environments where moderate levels of dissolved organic matter (FDOM) and low oxygenated water



predict higher fluxes (Figure 7d and Figure A1d). However, submerged bacterial mats along with filamentous green algae the presence of macrophytes and/or mosses in the lake and streams, were associated with lower fluxes, suggesting they form oxidative barriers for CH<sub>4</sub> fluxes from the sediment when submerged (Figure 7d and Figure A1d) (Heilman & Carlton, 2001; Laanbroek, 2010; Liebner et al., 2011; Esposito et al., 2023). The submerged, or not status of bacterial assemblages' points to an interesting feedback mechanism between CH<sub>4</sub> fluxes and dropping water levels creating variability in emission pathways. Similar processes have been shown in relation to submerged brown mosses in Arctic tundra ecosystems have been shown to promote CH<sub>4</sub> oxidation and thus decrease CH<sub>4</sub> emissions from sediments (Žárský et al., 2018). Overall, these results highlight the broader importance of fine-scale biogeochemical dynamics shaping CH<sub>4</sub> fluxes from a permafrost catchment and provide an important data point in an uncertain region of the world.

## 4 Conclusion

This research provides a temporally resolved catchment scale CH<sub>4</sub> flux analysis across different waterbody types and conditions—lake, streams, and ice/snow-covered surfaces—subsequently describing important biogeochemical and climatic controls on emissions. Often lost in temporally coarse assessments is a detailed understanding of seasonal transitions in processes related to CH<sub>4</sub> fluxes and environmental control mechanisms. Leveraging BRT to fit hundreds of randomized models and visualizing the direct, and indirect controls on CH<sub>4</sub> fluxes reveals variability in how, for example, DOM and/or water temperature affect fluxes differently as the Arctic summer progresses. We presented an approach which captures ecosystem-scale effects, but furthermore describes isolated mechanistic effects related to, for example, GPP, revealing that primary productivity plays a critical role in regulating CH<sub>4</sub> emissions from permafrost affected waterbodies. This work contributes to understanding carbon feedback mechanisms in a region where process-level knowledge is needed to scale global models simulating CH<sub>4</sub> emissions from permafrost affected waterbodies.

## Code Availability

R code for calculating methane fluxes can be found here: <https://github.com/mthayne527/fluxCH4>.

## Data Availability

Meteorological can be accessed here: <https://doi.org/10.17897/FEGK-0632>, and soil data here: <https://doi.org/10.17897/6G78-P793>, <https://doi.org/10.17897/9N7Z-GA63>, and can be accessed via the Greenland Ecosystem Monitoring website: <https://data.g-e-m.dk/datasets?theme=climate>. BAWLD circum-Arctic waterbody dataset can be found here: DOI: 10.5194/essd-13-5151-2021. Water chemistry and chamber data can be requested from Torsten Sachs at Helmholtz Centre for Geosciences in Potsdam, Germany (GFZ).

## Author contributions

MWT collected, compiled and analyzed data, and wrote the manuscript. KK collected, compiled, and analyzed data, and contributed writing parts of the manuscript. CW provided methodological guidance and feedback, and contributed to writing parts of the methodology. AK provided comments, feedback, and guidance on interpreting results, and contributed to writing various parts of the manuscript. TS collected data, provided comments, feedback, and guidance on interpreting results, and contributed to writing the manuscript.



## 548 Competing interests

549 The authors declare that they have no conflict of interest.

## 550 Acknowledgments

551 This research is part of the MOMENT project which is funded by the Federal Ministry of  
 552 Research, Technology and Space (BMFTR) under grant number 03F0931B. We acknowledge the  
 553 community of Qeqertarsuaq, Greenland for allowing us to research their land and water. We  
 554 acknowledge the help received from all of the partners part of the MOMENT project, with a specific  
 555 acknowledgment for Selina Undeutsch and Prof. Dr. Lars Kutzbach from the University of Hamburg.  
 556 We acknowledge Dr. Evan Wilcox for collecting water level from the lake during the 2024 field  
 557 season. We would acknowledge the University of Copenhagen and the Arctic Station team for  
 558 providing an environment for conducting this research. We acknowledge the work of the Greenland  
 559 Ecosystem Monitoring network and specifically Charlotte Sigsgaard for her help in getting  
 560 meteorological and soil data. ChatGPT models 4.1 and 5 were used to edit parts of the manuscript.

## 561 References

- 562 Bastviken, D., Cole, J., Pace, M., & Tranvik, L. (2004). Methane emissions from lakes:  
 563 Dependence of lake characteristics, two regional assessments, and a global estimate. *Global*  
 564 *Biogeochemical Cycles*, 18(4). <https://doi.org/10.1029/2004GB002238>  
 565
- 566 Bastviken, D., Cole, J. J., Pace, M. L., & van de-Bogert, M. C. (2008). Fates of methane from  
 567 different lake habitats: Connecting whole-lake budgets and CH<sub>4</sub> emissions. *Journal of*  
 568 *Geophysical Research: Biogeosciences*, 113(2). <https://doi.org/10.1029/2007JG000608>
- 569 Bartsch, A., Gay, B. A., Schüttemeyer, D., et al. (2025). Advancing the Arctic Methane  
 570 Permafrost Challenge (AMPAC) with future satellite missions. *IEEE Journal of Selected*  
 571 *Topics in Applied Earth Observations and Remote Sensing*, 15, 1234–1245. DOI:  
 572 10.1109/JSTARS.2025.3538897
- 573 Bogard, M. J., del Giorgio, P. A., Boutet, L., Chaves, M. C. G., Prairie, Y. T., Merante, A., &  
 574 Derry, A. M. (2014). Oxic water column methanogenesis as a major component of aquatic  
 575 CH<sub>4</sub> fluxes. *Nature Communications*, 5. <https://doi.org/10.1038/ncomms6350>
- 576 Bouranis, J. A., McGivern, B. B., Makke, G., et al. (2025). Metabolic redox coupling controls  
 577 methane production in permafrost-affected peatlands through organic matter  
 578 quality-dependent energy allocation. *Global Change Biology*, 31(8), e70390.  
 579 <https://doi.org/10.1111/gcb.70390>
- 580 Emerson, J. B., Varner, R. K., Wik, M., Parks, D. H., Neumann, R. B., Johnson, J. E.,  
 581 Singleton, C. M., Woodcroft, B. J., Tollerson, R., Owusu-Dommey, A., Binder, M., Freitas,  
 582 N. L., Crill, P. M., Saleska, S. R., Tyson, G. W., & Rich, V. I. (2021). Diverse sediment  
 583 microbiota shape methane emission temperature sensitivity in Arctic lakes. *Nature*  
 584 *Communications*, 12(1). <https://doi.org/10.1038/s41467-021-25983-9>  
 585
- 586 Callaghan, T. v., Christensen, T. R., & Jantze, E. J. (2011). Plant and vegetation dynamics on  
 587 Disko island, west Greenland: Snapshots separated by over 40 years. In *Ambio* (Vol. 40, Issue  
 588 6). <https://doi.org/10.1007/s13280-011-0169-x>





- 589 Cheng, S., Meng, F., Wang, Y., Zhang, J., & Zhang, L. (2024). The potential linkage between  
590 sediment oxygen demand and microbes and its contribution to the dissolved oxygen depletion  
591 in the Gan River. *Frontiers in Microbiology*, 15, 1413447.  
592 <https://doi.org/10.3389/fmicb.2024.1413447>
- 593 Christiansen, H. H. (1999). Active layer monitoring in two Greenlandic permafrost areas:  
594 Zackenberg and Disko Island. *Geografisk Tidsskrift*, 99.  
595
- 596 Christiansen, J. R., Romero, A. J. B., Jørgensen, N. O. G., Glaring, M. A., Jørgensen, C. J.,  
597 Berg, L. K., & Elberling, B. (2015). Methane fluxes and the functional groups of  
598 methanotrophs and methanogens in a young Arctic landscape on Disko Island, West  
599 Greenland. *Biogeochemistry*, 122(1). <https://doi.org/10.1007/s10533-014-0026-7>  
600
- 601 Cole, J. J., & Caraco, N. F. (1998). Atmospheric exchange of carbon dioxide in a low-wind  
602 oligotrophic lake measured by the addition of SF<sub>6</sub>. *Limnology and Oceanography*, 43(4).  
603 <https://doi.org/10.4319/lo.1998.43.4.0647>  
604 Conrad, R. (2007). Microbial Ecology of Methanogens and Methanotrophs. In *Advances in*  
605 *Agronomy* (Vol. 96). [https://doi.org/10.1016/S0065-2113\(07\)96005-8](https://doi.org/10.1016/S0065-2113(07)96005-8)
- 606 Cunada, C. L., Lesack, L. F. W., Tank, S. E., & Hesslein, R. H. (2021). Methane flux  
607 dynamics among CO<sub>2</sub>-absorbing and thermokarst lakes of a great Arctic delta.  
608 *Biogeochemistry*, 156(1), 25–39. <https://doi.org/10.1007/s10533-021-00853-0>
- 609 D’Imperio, L., Nielsen, C. S., Westergaard-Nielsen, A., Michelsen, A., & Elberling, B.  
610 (2017). Methane oxidation in contrasting soil types: responses to experimental warming with  
611 implication for landscape-integrated CH<sub>4</sub> budget. *Global Change Biology*, 23(2).  
612 <https://doi.org/10.1111/gcb.13400>  
613
- 614 Elder, C. D., Thompson, D. R., Thorpe, A. K., Hanke, P., Walter Anthony, K. M., & Miller,  
615 C. E. (2020). Airborne Mapping Reveals Emergent Power Law of Arctic Methane Emissions.  
616 *Geophysical Research Letters*, 47(3). <https://doi.org/10.1029/2019GL085707>  
617
- 618 Elith, J., Leathwick, J. R., & Hastie, T. (2008). A working guide to boosted regression trees.  
619 In *Journal of Animal Ecology* (Vol. 77, Issue 4). <https://doi.org/10.1111/j.1365-2656.2008.01390.x>  
620
- 621 Emerson, J. B., Varner, R. K., Wik, M., Parks, D. H., Neumann, R. B., Johnson, J. E.,  
622 Singleton, C. M., Woodcroft, B. J., Tollerson, R., Owusu-Dommey, A., Binder, M., Freitas,  
623 N. L., Crill, P. M., Saleska, S. R., Tyson, G. W., & Rich, V. I. (2021). Diverse sediment  
624 microbiota shape methane emission temperature sensitivity in Arctic lakes. *Nature*  
625 *Communications*, 12(1). <https://doi.org/10.1038/s41467-021-25983-9>  
626
- 627 Esposito, C., Nijman, T. P. A., Veraart, A. J., Audet, J., Levi, E. E., Lauridsen, T. L., &  
628 Davidson, T. A. (2023). Activity and abundance of methane-oxidizing bacteria on plants in  
629 experimental lakes subjected to different nutrient and warming treatments. *Aquatic Botany*,  
630 185. <https://doi.org/10.1016/j.aquabot.2022.103610>  
631
- 632 Fazi, S., Amalfitano, S., Venturi, S., Pacini, N., Vazquez, E., Olaka, L. A., Tassi, F.,  
633 Crognale, S., Herzsprung, P., Lechtenfeld, O. J., Cabassi, J., Capecchiacci, F., Rossetti, S.,  
634 Yakimov, M. M., Vaselli, O., Harper, D. M., & Butturini, A. (2021). High concentrations of  
635



- 636 dissolved biogenic methane associated with cyanobacterial blooms in East African lake  
637 surface water. *Communications Biology*, 4(1). <https://doi.org/10.1038/s42003-021-02365-x>
- 638 Fox-Kemper, B., Hewitt, H. T., Xiao, C., et al. (2021). Chapter 9: Ocean, cryosphere and sea  
639 level change. In: *Climate Change 2021: The Physical Science Basis. Contribution of Working*  
640 *Group I to the Sixth Assessment Report of the Intergovernmental Panel on Climate Change.*  
641 *Cambridge University Press*, 1211–1362. <https://doi.org/10.1017/9781009157896.011>
- 642 Garcia, H. E., & Gordon, L. I. (1992). Oxygen solubility in seawater: Better fitting equations.  
643 In *Limnology and Oceanography* (Vol. 37, Issue 6).  
644 <https://doi.org/10.4319/lo.1992.37.6.1307>  
645
- 646 Graef, C., Hestnes, A. G., Svenning, M. M., & Frenzel, P. (2011). The active methanotrophic  
647 community in a wetland from the High Arctic. *Environmental Microbiology Reports*, 3(4).  
648 <https://doi.org/10.1111/j.1758-2229.2010.00237.x>  
649
- 650 Hall, R. O., & Madinger, H. L. (2018). Use of argon to measure gas exchange in turbulent  
651 mountain streams. *Biogeosciences*, 15(10). <https://doi.org/10.5194/bg-15-3085-2018>
- 652 Heilman, M. A., & Carlton, R. G. (2001). Methane oxidation associated with submersed  
653 vascular macrophytes and its impact on plant diffusive methane flux. *Biogeochemistry*, 52(2),  
654 207–224. DOI: 10.1023/A:1006427712846
- 655 Hijmans RJ, Phillips S, Leathwick J, Elith J (2023). *dismo: Species Distribution Modeling*. R  
656 package version 1.3-14. DOI: 10.32614/CRAN.package.dismo
- 657 Hoffmann, M., Schulz-Hanke, M., Garcia Alba, J., Jurisch, N., Hagemann, U., Sachs, T.,  
658 Sommer, M., & Augustin, J. (2017). A simple calculation algorithm to separate high-  
659 resolution CH<sub>4</sub> flux measurements into ebullition- and diffusion-derived components.  
660 *Atmospheric Measurement Techniques*, 10(1). <https://doi.org/10.5194/amt-10-109-2017>  
661
- 662 Humlum, O. (1998). Active layer thermal regime 1991–1996 at Qeqertarsuaq, Disko Island,  
663 Central West Greenland. *Arctic and Alpine Research*, 30(3). <https://doi.org/10.2307/1551977>  
664
- 665 Humlum, O., Hansen, B. U., & Nielsen, N. (1999). Meteorological observations 1998 at the  
666 arctic station, Qeqertarsuaq (69°15'N), Central West Greenland. *Geografisk Tidsskrift*, 99.  
667 <https://doi.org/10.1080/00167223.1999.10649428>
- 668 Iannone R, Roy O (2024). *\_DiagrammeR: Graph/Network Visualization\_*. R package version  
669 1.0.11. DOI: 10.32614/CRAN.package.DiagrammeR
- 670 Juncher Jørgensen, C., Schlaikjær Mariager, T., & Riis Christiansen, J. (2024). Spatial  
671 variation of net methane uptake in Arctic and subarctic drylands of Canada and Greenland.  
672 *Geoderma*, 443. <https://doi.org/10.1016/j.geoderma.2024.116815>  
673
- 674 Keskitalo, K. H., Bröder, L., Shakil, S., Zolkos, S., Tank, S. E., van Dongen, B. E., Tesi, T.,  
675 Haghipour, N., Eglinton, T. I., Kokelj, S. v., & Vonk, J. E. (2021). Downstream Evolution of  
676 Particulate Organic Matter Composition From Permafrost Thaw Slumps. *Frontiers in Earth*  
677 *Science*, 9. <https://doi.org/10.3389/feart.2021.642675>  
678



- 679 Kleber, G. E., Magerl, L., Turchyn, A. V., Schloemer, S., Trimmer, M., Zhu, Y., & Hodson,  
680 A. (2025). Proglacial methane emissions driven by meltwater and groundwater flushing in a  
681 high-Arctic glacial catchment. *Biogeosciences*, 22(3), 659–674. [https://doi.org/10.5194/bg-](https://doi.org/10.5194/bg-22-659-2025)  
682 22-659-2025
- 683
- 684 Kluge, M., Wauthy, M., Clemmensen, K. E., Wurzbacher, C., Hawkes, J. A., Einarsdottir, K.,  
685 Rautio, M., Stenlid, J., & Peura, S. (2021). Declining fungal diversity in Arctic freshwaters  
686 along a permafrost thaw gradient. *Global Change Biology*, 27(22).  
687 <https://doi.org/10.1111/gcb.15852>
- 688
- 689 Korrensalo, A., Alekseychik, P., Mammarella, I., et al. (2024). High-resolution spatial  
690 patterns and drivers of terrestrial ecosystem greenhouse gas fluxes in sub-Arctic Finland.  
691 *Biogeosciences*, 21, 335–352. <https://doi.org/10.5194/bg-21-335-2024>
- 692 Kuhn, M. A., Varner, R. K., Bastviken, D., Crill, P., MacIntyre, S., Turetsky, M., Walter  
693 Anthony, K., McGuire, A. D., and Olefeldt, D. (2021). BAWLD-CH4: a comprehensive  
694 dataset of methane fluxes from boreal and arctic ecosystems, *Earth System Science Data*, 13,  
695 5151–5189. DOI: 10.5194/essd-13-5151-2021
- 696 Kutzbach, L., Schneider, J., Sachs, T., Giebels, M., Nykänen, H., Shurpali, N. J.,  
697 Martikainen, P. J., Alm, J., & Wilmking, M. (2007). CO<sub>2</sub> flux determination by closed-  
698 chamber methods can be seriously biased by inappropriate application of linear regression.  
699 *Biogeosciences*, 4(6). <https://doi.org/10.5194/bg-4-1005-2007>
- 700
- 701 Laanbroek, H. J. (2010). Methane emission from natural wetlands: Interplay between  
702 emergent macrophytes and soil microbial processes. A mini-review. In *Annals of Botany*  
703 105(1). <https://doi.org/10.1093/aob/mcp201>
- 704
- 705 Larsen, J. G., & Larsen, L. M. (2022). Lithostratigraphy, geology and geochemistry of the  
706 Tertiary volcanic rocks on Svartenhuk Halvø and adjoining areas, West Greenland. *GEUS*  
707 *Bulletin*, 50. <https://doi.org/10.34194/geusb.v50.8295>
- 708
- 709 Liebner, S., Zeyer, J., Wagner, D., Schubert, C., Pfeiffer, E. M., & Knoblauch, C. (2011).  
710 Methane oxidation associated with submerged brown mosses reduces methane emissions  
711 from Siberian polygonal tundra. *Journal of Ecology*, 99(4). [https://doi.org/10.1111/j.1365-](https://doi.org/10.1111/j.1365-2745.2011.01823.x)  
712 2745.2011.01823.x
- 713
- 714 Michel, G., Tonon, T., Scornet, D., Cock, J. M., & Kloareg, B. (2010). Central and storage  
715 carbon metabolism of the brown alga *Ectocarpus siliculosus*: Insights into the origin and  
716 evolution of storage carbohydrates in Eukaryotes. *New Phytologist*, 188(1).  
717 <https://doi.org/10.1111/j.1469-8137.2010.03345.x>
- 718
- 719 Miner, K. R., Turetsky, M. R., Malina, E., Bartsch, A., Tamminen, J., McGuire, A. D., Fix,  
720 A., Sweeney, C., Elder, C. D., & Miller, C. E. (2022). Permafrost carbon emissions in a  
721 changing Arctic. In *Nature Reviews Earth and Environment* (Vol. 3, Issue 1).  
722
- 723 Mulholland, P. J., Fellows, C. S., Tank, J. L., Grimm, N. B., Webster, J. R., Hamilton, S. K.,  
724 Martí, E., Ashkenas, L., Bowden, W. B., Dodds, W. K., McDowell, W. H., Paul, M. J., &  
725 Peterson, B. J. (2001). Inter-biome comparison of factors controlling stream metabolism.  
726 *Freshwater Biology*, 46(11). <https://doi.org/10.1046/j.1365-2427.2001.00773.x>



- 727 <https://doi.org/10.1038/s43017-021-00230-3>  
728
- 729 Neumann, R. B., Moorberg, C. J., Lundquist, J. D., Turner, J. C., Waldrop, M. P., McFarland,  
730 J. W., Euskirchen, E. S., Edgar, C. W., & Turetsky, M. R. (2019). Warming Effects of Spring  
731 Rainfall Increase Methane Emissions From Thawing Permafrost. *Geophysical Research*  
732 *Letters*, 46(3). <https://doi.org/10.1029/2018GL081274>  
733
- 734 Noss, C., Bodmer, P., Koca, K., & Lorke, A. (2018). Flow and Turbulence driven Water  
735 Surface Roughness and Gas Exchange Velocity in Streams. *E3S Web of Conferences*, 40.  
736 <https://doi.org/10.1051/e3sconf/20184005018>  
737
- 738 Olefeldt, D., Hovemyr, M., Kuhn, M. A., Bastviken, D., Bohn, T. J., Connolly, J., Crill, P.,  
739 Euskirchen, E. S., Finkelstein, S. A., Genet, H., Grosse, G., Harris, L. I., Heffernan, L.,  
740 Helbig, M., Hugelius, G., Hutchins, R., Juutinen, S., Lara, M. J., Malhotra, A., ... Watts, J. D.  
741 (2021). The boreal-arctic wetland and lake dataset (BAWLD). *Earth System Science Data*,  
742 13(11). <https://doi.org/10.5194/essd-13-5127-2021>  
743
- 744 Olid, C., Zannella, A., & Lau, D. C. P. (2021). The Role of Methane Transport From the  
745 Active Layer in Sustaining Methane Emissions and Food Chains in Subarctic Ponds. *Journal*  
746 *of Geophysical Research: Biogeosciences*, 126(3). <https://doi.org/10.1029/2020JG005810>  
747
- 748 Olid, C., Rodellas, V., Rocher-Ros, G., Garcia-Orellana, J., Diego-Feliu, M., Alorda-  
749 Kleinglass, A., Bastviken, D., & Karlsson, J. (2022). Groundwater discharge as a driver of  
750 methane emissions from Arctic lakes. *Nature Communications*, 13(1).  
751 <https://doi.org/10.1038/s41467-022-31219-1>  
752
- 753 Pedersen, A. R., Petersen, S. O., & Schelde, K. (2010). A comprehensive approach to soil-  
754 atmosphere trace-gas flux estimation with static chambers. *European Journal of Soil Science*,  
755 61(6). <https://doi.org/10.1111/j.1365-2389.2010.01291.x>  
756
- 757 QGIS Development Team: QGIS Geographic Information System, Open Source Geospatial  
758 Foundation Project, available at: <https://qgis.org>  
759
- 760 Rautio, M., Dufresne, F., Laurion, I., Bonilla, S., Vincent, W. F., & Christoffersen, K. S.  
761 (2011). Shallow freshwater ecosystems of the circumpolar Arctic. *Ecoscience*, 18(3).  
762 <https://doi.org/10.2980/18-3-3463>
- 763 Ravn, N. R., Elberling, B., & Michelsen, A. (2020). Arctic soil carbon turnover controlled by  
764 experimental snow addition, summer warming and shrub removal. *Soil Biology and*  
765 *Biochemistry*, 142. <https://doi.org/10.1016/j.soilbio.2019.107698>
- 766 Saunois, M., R. Stavert, A., Poulter, B., Bousquet, P., G. Canadell, J., B. Jackson, R., A.  
767 Raymond, P., J. Dlugokencky, E., Houweling, S., K. Patra, P., Ciais, P., K. Arora, V.,  
768 Bastviken, D., Bergamaschi, P., R. Blake, D., Brailsford, G., Bruhwiler, L., M. Carlson, K.,  
769 Carrol, M., ... Zhuang, Q. (2020). The global methane budget 2000-2017. *Earth System*  
770 *Science Data*, 12(3). <https://doi.org/10.5194/essd-12-1561-2020>  
771
- 772 Schuur, E. A. G., McGuire, A. D., Schädel, C., Grosse, G., Harden, J. W., Hayes, D. J.,  
773 Hugelius, G., Koven, C. D., Kuhry, P., Lawrence, D. M., Natali, S. M., Olefeldt, D.,  
774 Romanovsky, V. E., Schaefer, K., Turetsky, M. R., Treat, C. C., & Vonk, J. E. (2015).



- 775 Climate change and the permafrost carbon feedback. In *Nature* (Vol. 520, Issue 7546).  
776 <https://doi.org/10.1038/nature14338>  
777
- 778 Singleton, C. M., McCalley, C. K., Woodcroft, B. J., Boyd, J. A., Evans, P. N., Hodgkins, S.  
779 B., Chanton, J. P., Frolking, S., Crill, P. M., Saleska, S. R., Rich, V. I., & Tyson, G. W.  
780 (2018). Methanotrophy across a natural permafrost thaw environment. *ISME Journal*, 12(10).  
781 <https://doi.org/10.1038/s41396-018-0065-5>  
782
- 783 Street, L. E., Dean, J. F., Billett, M. F., Baxter, R., Dinsmore, K. J., Lessels, J. S., Subke, J.  
784 A., Tetzlaff, D., & Wookey, P. A. (2016). Redox dynamics in the active layer of an Arctic  
785 headwater catchment; examining the potential for transfer of dissolved methane from soils to  
786 stream water. *Journal of Geophysical Research: Biogeosciences*, 121(11).  
787 <https://doi.org/10.1002/2016JG003387>  
788
- 789 Stevenson, M. A., McGowan, S., Pearson, E. J., Swann, G. E. A., Leng, M. J., Jones, V. J.,  
790 Bailey, J. J., Huang, X., & Whiteford, E. (2021). Anthropocene climate warming enhances  
791 autochthonous carbon cycling in an upland Arctic lake, Disko Island, West Greenland.  
792 *Biogeosciences*, 18(8). <https://doi.org/10.5194/bg-18-2465-2021>  
793
- 794 Virkkala, A. M., Niittynen, P., Kemppinen, J., Marushchak, M. E., Voigt, C., Hensgens, G.,  
795 Kerttula, J., Happonen, K., Tyystjärvi, V., Biasi, C., Hultman, J., Rinne, J., & Luoto, M.  
796 (2024). High-resolution spatial patterns and drivers of terrestrial ecosystem carbon dioxide,  
797 methane, and nitrous oxide fluxes in the tundra. *Biogeosciences*, 21(2).  
798 <https://doi.org/10.5194/bg-21-335-2024>  
799
- 800 Walter Anthony, K. M., Anthony, P., Grosse, G., & Chanton, J. (2012). Geologic methane  
801 seeps along boundaries of Arctic permafrost thaw and melting glaciers. *Nature Geoscience*,  
802 5(6). <https://doi.org/10.1038/ngeo1480>  
803
- 804 Walter Anthony, K., Schneider von Deimling, T., Nitze, I., Frolking, S., Emond, A., Daanen,  
805 R., Anthony, P., Lindgren, P., Jones, B., & Grosse, G. (2018). 21st-century modeled  
806 permafrost carbon emissions accelerated by abrupt thaw beneath lakes. *Nature*  
807 *Communications*, 9(1). <https://doi.org/10.1038/s41467-018-05738-9>  
808
- 809 Walvoord, M. A., & Kurylyk, B. L. (2016). Hydrologic Impacts of Thawing Permafrost—A  
810 Review. *Vadose Zone Journal*, 15(6). <https://doi.org/10.2136/vzj2016.01.0010>  
811
- 812 Wallenius, A. J., Dalcin Martins, P., Slomp, C. P., & Jetten, M. S. M. (2021). Anthropogenic  
813 and Environmental Constraints on the Microbial Methane Cycle in Coastal Sediments. In  
814 *Frontiers in Microbiology* (Vol. 12). <https://doi.org/10.3389/fmicb.2021.631621>  
815
- 816 Westergaard-Nielsen, A., Balstrøm, T., Treier, U. A., Normand, S., & Elberling, B. (2020).  
817 Estimating meltwater retention and associated nitrate redistribution during snowmelt in an  
818 Arctic tundra landscape. *Environmental Research Letters*, 15(3).  
819 <https://doi.org/10.1088/1748-9326/ab57b1>
- 820 Winslow, L. A., Zwart, J. A., Batt, R. D., Dugan, H. A., Woolway, R. I., Corman, J. R.,  
821 Hanson, P. C., & Read, J. S. (2016). LakeMetabolizer: an R package for estimating lake  
822 metabolism from free-water oxygen using diverse statistical models. *Inland Waters*, 6(4).  
823 <https://doi.org/10.1080/IW-6.4.883>

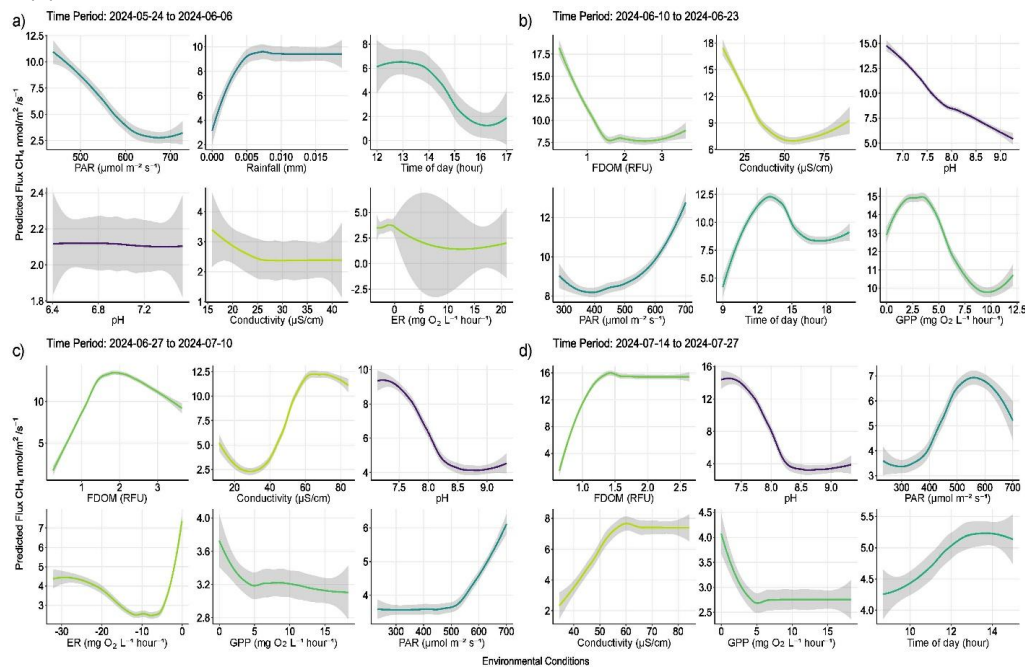




- 824 H. Wickham. ggplot2: Elegant Graphics for Data Analysis. Springer-Verlag New York, 2016.  
 825 DOI: 10.1007/978-3-319-24277-4
- 826 Xu, W., Lambæk, A., Holm, S. S., Furbo-Halken, A., Elberling, B., & Ambus, P. L. (2021).  
 827 Effects of experimental fire in combination with climate warming on greenhouse gas fluxes  
 828 in Arctic tundra soils. *Science of the Total Environment*, 795.  
 829 <https://doi.org/10.1016/j.scitotenv.2021.148847>
- 830  
 831 Yuan, K., Li, F., McNicol, G., Chen, M., Hoyt, A., Knox, S., Riley, W. J., Jackson, R., &  
 832 Zhu, Q. (2024). Boreal–Arctic wetland methane emissions modulated by warming and  
 833 vegetation activity. *Nature Climate Change*, 14(3). [https://doi.org/10.1038/s41558-024-](https://doi.org/10.1038/s41558-024-01933-3)  
 834 01933-3
- 835  
 836 Žárský, J. D., Kohler, T. J., Yde, J. C., Falteisek, L., Lamarche-Gagnon, G., Hawkings, J. R.,  
 837 Hatton, J. E., & Stibal, M. (2018). Prokaryotic assemblages in suspended and subglacial  
 838 sediments within a glacierized catchment on Qeqertarsuaq (Disko Island), west Greenland.  
 839 *FEMS Microbiology Ecology*, 94(7). <https://doi.org/10.1093/femsec/fiy100>
- 840 Zastruzny, S. F., Elberling, B., Nielsen, L., & Jensen, K. H. (2017). Water flow in the active  
 841 layer along an arctic slope—An investigation based on a field campaign and model  
 842 simulations. *The Cryosphere Discussions*, 1-32.
- 843



844 **Appendix A**



845

846 Figure A1. Partial dependency plots illustrating predicted marginal effects of meteorological, and  
847 biochemical water conditions predicting diffusive CH<sub>4</sub> fluxes. Each figure represents the direct  
848 marginal effect on CH<sub>4</sub> fluxes when all other predictors are held at their median, therefore giving a  
849 more mechanistic understanding of those conditions and processes regulating fluxes from water  
850 surfaces. The figures are ordered by importance in each time period and colors correspond to those  
851 seen in Figure 6 of the main text. The colored lines represent the result of a fitted general additive  
852 model ( $y \sim s(x)$ ) and thus a smooth representation across the 321 fitted BRT models. Each predictor  
853 and its numerical range are given on the x-axis, while predicted fluxes are given on the y-axis.

854



Figure A2. Illustrates the various microbial forms encountered and found to influence  $\text{CH}_4$  fluxes from the catchment area. In the photo on the far left we can see gas film on the water surface which was associated with submerged iron-oxidizing microbial assemblages, i.e. similar to what is shown in the middle photo, however exposed to the atmosphere in lower water levels. The photo on the right shows a brown alga which formed in the warm spring area southeast of the lake. In all cases, increased fluxes were generally encountered when measuring atop the middle and right microbial assemblages.